

VU Research Portal

Validating the performance of a Raman laser spectrometer (RLS) instrument under Martian conditions

Motamedi Mohammadabadi, K.

2013

document version

Publisher's PDF, also known as Version of record

[Link to publication in VU Research Portal](#)

citation for published version (APA)

Motamedi Mohammadabadi, K. (2013). *Validating the performance of a Raman laser spectrometer (RLS) instrument under Martian conditions*. [PhD-Thesis - Research and graduation internal, Vrije Universiteit Amsterdam].

General rights

Copyright and moral rights for the publications made accessible in the public portal are retained by the authors and/or other copyright owners and it is a condition of accessing publications that users recognise and abide by the legal requirements associated with these rights.

- Users may download and print one copy of any publication from the public portal for the purpose of private study or research.
- You may not further distribute the material or use it for any profit-making activity or commercial gain
- You may freely distribute the URL identifying the publication in the public portal

Take down policy

If you believe that this document breaches copyright please contact us providing details, and we will remove access to the work immediately and investigate your claim.

E-mail address:

vuresearchportal.ub@vu.nl

Chapter 2: Raman and Laser induced breakdown Spectrometer (RLS)

Contents

2.1	Introduction.....	42
2.2	Principles of Raman spectroscopy.....	42
2.2.1	The Raman effect.....	43
2.2.2	Raman intensity.....	46
2.2.3	Number of normal modes of vibration.....	47
2.2.4	Vibrational dynamics of molecules and solid crystalline.....	47
2.2.5	Advantages and disadvantages of Raman Spectroscopy.....	49
2.3	Laser induced breakdown spectroscopy (LIBS).....	50
2.3.1	History of LIBS spectroscopy.....	51
2.3.2	The basic principles of LIBS.....	51
2.3.3	Advantages and disadvantages of LIBS spectroscopy.....	53
2.4	The RLS instrument.....	53
2.4.1	Laser sources.....	54
2.4.1.1	Raman laser source.....	54
2.4.1.2	LIBS laser source.....	59
2.4.2	Optical head.....	59
2.4.3	Spectrometer.....	61
2.5	Characteristics of the RLS instrument.....	66
2.5.1	Instrument resolution.....	66
2.5.2	Calibration of the CCD at different temperatures.....	67
2.5.2.1	White light to determine position of the third order.....	67
2.5.2.2	Calibration of the CCD column number to wavelength.....	69
2.5.2.3	Accuracy of Raman shift values.....	72
2.5.3	CCD noise and the detection limit of Raman signals.....	76
2.6	Conclusion.....	77
2.7	References.....	79

2.1 Introduction

The European space agency (ESA) instrument that was used during this PhD research study is a combined Raman and Laser-induced breakdown spectroscopy (LIBS) (RLS) instrument. It was initially designed by TNO (Nederlandse Organisatie voor Toegepast Natuurwetenschappelijk Onderzoek or Dutch Organization for Applied Scientific Research) as an elegant breadboard (EB) for the ExoMars mission. EB refers to equipment before it reaches the stage of engineering mode (EM). It is built using commercial grade components and a configuration close to that of the flight mode (FM).

At the beginning of the ExoMars mission program, this instrument had a high priority within the scientific community and had been chosen as one of the main instruments for ExoMars mission that would act as the first contact with Martian samples. However, due to the economic crisis, governments spent less money on space projects. ESA was affected and set new requirements such as less weight for the instruments aboard the ExoMars mission. The RLS instrument was therefore required to be lighter in order to fit within the mission budget. After extensive review, the LIBS capability was removed from the RLS instrument. Only a Raman spectrometer will be included in the scheduled ExoMars mission in 2018.

After initial testing at TNO, the RLS instrument was delivered to the instrument principal investigator (PI) in Spain. An agreement was made for subsequent delivery to the Vrije University Amsterdam. It arrived in 2011 after more than two years delay. One of its optical fibres was found damaged. The first step before assessing the capabilities of the RLS instrument was to repair the optical fibre of the spectrometer and to optimize its performance. The aim was to do this as quickly as possible and at the lowest cost possible.

Based on the changing size of the instrument and the changed goals of the ExoMars mission to a Raman only spectrometer, the focus of this PhD research was changed. The subject of the PhD was narrowed to the study of the performances of the Raman laser spectrometer only, including the influence of Mars' surface conditions on the Raman spectra of selected minerals. However, the design of the RLS instrument incorporates both Raman and LIBS capabilities. Consequently, in this chapter the basic theory of Raman and LIBS spectroscopy, the design of the instrument and its technical performance under Martian conditions are discussed. This chapter includes the development undertaken during this PhD to improve the instrument stability (for instance: laser stability, cooling of the spectrometer charge-coupled device (CCD)). Note that the LIBS technique and instrument design are briefly introduced because the performances of the Raman instrument are partly linked to the specific combined Raman-LIBS design. Finally, the results of the spectrometer calibration at different temperatures are presented in the last section of this chapter.

2.2 Principles of Raman spectroscopy

In order to interpret the data collected by the Raman spectrometer one must first understand the interactions between light and samples. The objective of this section is not to provide the full theory of Raman spectroscopy using quantum mechanics but to give the information

necessary for understanding and interpreting Raman data in space applications (for more information the reader can refer to the book "Raman spectroscopy applied to Earth science and culture heritage", edited by Dubessy et al., (2012).

The first section focuses on the classical theory of Raman spectroscopy. Subsequently, the intensity of Raman scattering is explained followed by the dynamics of molecules (described by harmonic oscillators). Then, an introduction to normal modes of vibration is provided. Finally, vibrational dynamics of molecules and solid crystalline materials are explained.

2.2.1 The Raman effect

In 1923, Adolf Smekal predicted the existence of inelastic scattering by quantum mechanical calculations (Smekal, 1923). Four years later, Krishnan and Raman provided the practical evidence of this inelastic scattering of light. This scattering was called the Raman effect (Raman, and Krishnan 1928).

Unlike Rayleigh scattering, which corresponds to an elastic scattering of light (Rayleigh, 1899), Raman scattering is inelastic scattering of light due to various elementary excitations where the energy is lost or gained during the scattering process. These excitations may be the internal vibration modes in:

- a) A molecule (vibrons or intermolecular vibration)
- b) Phonons in an ordered crystal structure (lattice vibrations or external vibrations). A phonon is an elementary vibrational motion in which a lattice of atoms or molecules uniformly oscillates at a single frequency
- c) Magnons in systems with magnetic-order transitions. Magnon or spin wave is a wave, propagated through a crystal lattice as a result of changes in the spin angular momentum of electrons in the lattice

For Raman spectroscopy, a monochromatic laser beam (ν_0) is directed to a sample. The light interacts with the sample and is partly scattered. The scattered lights can be classified into two categories:

- a) Rayleigh scattering: Rayleigh elastic scattering is strong compared to Raman scattering (Raman scattering is about 0.001% of the incident beam) and has the same frequency as the incident beam (ν_0)
- b) Raman scattering: Raman scattering or inelastic scattering is very weak and has the frequencies $\nu_0 + \nu_m$ or $\nu_0 - \nu_m$, where ν_m is a vibrational frequency of a molecule. The $\nu_0 + \nu_m$ and $\nu_0 - \nu_m$ frequencies are referred to as the anti-Stokes and Stokes peaks respectively

Raman shift is expressed as a wavenumber in units of inverse centimetres. The laser excitation light is used as a reference and therefore has a Raman shift of zero. Raman shift values are not specifically dependent on the laser excitation wavelength.

In order to convert from spectral wavelength to Raman shift (in wavenumber) in the Raman spectrum, the following equation is applied:

$$\Delta\omega \sim \left(\frac{1}{\lambda_0} - \frac{1}{\lambda_1} \right) \quad (2.1)$$

where $\Delta\omega$ is the Raman shift in wavenumber, λ_0 is the excitation wavelength, and λ_1 is wavelength of the scattered light. Wavelength is usually expressed in nanometres (nm) and Raman shifts in cm^{-1} . Then:

$$\Delta\omega(\text{cm}^{-1}) = \left(\frac{1}{\lambda_0(\text{nm})} - \frac{1}{\lambda_1(\text{nm})} \right) \times 10^7 \quad (2.2)$$

Figure 2.1 shows a Jablonski diagram for Raman scattering. The figure illustrates the electronic states of a molecule and the transitions between its electronic states. Most molecules are present in the ground electronic state (m state) at room temperature. When the laser interacts with the electrons in a molecular bond, virtual states, which are not the real states of the molecule, are created. Most photons scatter by a Rayleigh process. As light is reflected with the same energy, the Rayleigh process does not involve any energy change. In Stokes scattering, a molecule (in state m) absorbs energy and is excited to a higher energy vibrational state (n). However, depending on the ambient temperature, some molecules in the material will already exist in a higher energy excited vibrational state (n state) (Fig. 2.1). Scattering from these states to the ground state m is called anti-Stokes scattering. The population of molecules at state m is much larger than at state n. The relative intensities of the Stokes and anti-Stokes scattering depend on the population of the various states of the molecule. Therefore, anti-Stokes scattering is usually weaker than Stokes scattering in ambient conditions. As both processes give the same information about the characteristic energy levels within a molecule, it is more common to only measure the Stokes scattering.

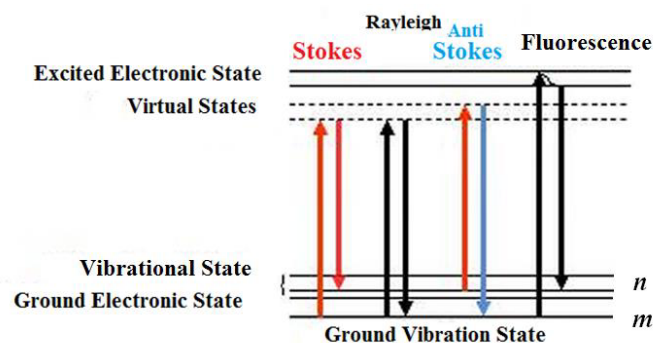


Figure. 2.1. Jablonski diagram showing the different processes and the states involved in different light molecule interaction: Stokes Raman scattering, Rayleigh scattering, Anti-Stokes Raman scattering and fluorescence. Modified from http://biomed.tamu.edu/obs/OBSL/Research%20Projects/SERS_biosensor.htm

The Raman and fluorescence process is shown in the Jablonski diagram (Fig. 2.1). In the fluorescence process, a molecule is first excited from its ground electronic state to one of the various vibrational states in the excited electronic state by absorbing a photon. Collisions

with other molecules cause the excited molecule to rapidly lose vibrational energy until it reaches the lowest vibrational state of the first excited electronic state. When the energy of the excitation wavelength (incident photons) is equal to the energy difference between ground energy state and one of the excited states of the molecule, Raman scattering sometimes overlaps with fluorescence. Fluorescence influences the overall quality of Raman spectra as it appears as a broad background.

Willes and Merlin (2000) and Lewis and Edwards (2001) explained the Raman scattering process in terms of the effect of an electric field on a molecule. When a molecule is affected by an electric field, the dipolar moment of the molecule μ is given by:

$$\mu = \mu_o + \alpha E \quad (2.3)$$

where μ_o is the permanent dipole moment. The molecule has an electric dipole moment when it has a net separation of centres of positive and negative charges. A permanent electric dipole moment exists if the separation of charge is a characteristic of the molecule without the use of an external electric field.

αE is the induced dipolar moment: When a polarisable molecule (that did not have a permanent electric dipole moment) is subject to an electric field, the temporary distortion of the electron cloud around a certain molecular bond creates an induced electric dipole moment in the molecule.

When a molecule interacts with the electric field $E = E_o \cos\omega t$, the small vibrations of the molecule are given by $q_n(t)$, where $q_n(t) = q_{no} \cos(\omega t)$ (q_{no} is the amplitude and ω_n is the vibration frequency of the normal mode n). Therefore, based on the equation (2.3), the total dipolar moment is described as follows:

$$\begin{aligned} \mu = & \mu_o + \alpha(0)E_o \cos(\omega t) + \sum_{n=1}^0 \left(\frac{\partial \mu}{\partial q_n}\right)_0 q_{no} \cos(\omega_0 t) \\ & + \frac{1}{2} E_o \sum_{n=1}^0 \left(\frac{\partial \alpha}{\partial q_n}\right)_0 q_{no} [\cos(\omega + \omega_n)t + \cos(\omega - \omega_n)t] \end{aligned} \quad (2.4)$$

Where a power series expansion of q_n , μ and α have been made and only the first terms are taken into account. The second and third terms in equation 2.4 correspond to the Rayleigh and the infrared processes (infrared spectrum is based on absorption spectroscopy and is beyond the scope of this study). The last term describes the Raman scattering (anti-Stokes and Stokes terms). Consequently, if $\left.\frac{\partial \alpha}{\partial q}\right|_{q=0}$ is zero, the molecular vibration is not Raman

active. To be Raman active, the rate of change of polarizability α with vibration cannot be zero and in a Raman spectrum only those vibrations are detected that result in a change in polarizability. A more detailed explanation of the subject can be found in the book "Raman spectroscopy applied to Earth science and culture heritage", edited by Dubessy et al., (2012).

2.2.2 Raman intensity

A Raman spectrum is a plot of the intensity of Raman scattered radiation as a function of its frequency difference from the incident radiation (in units of wavenumbers, cm^{-1}). As mentioned before, this difference is called the Raman shift. Figure 2.2 shows the Raman spectrum of calcite as an example. The intensities of the different peaks depend in a complex way on the polarizability of the molecule, the intensity of the source and the concentration of the Raman active group in the sample structure (equation 2.5).

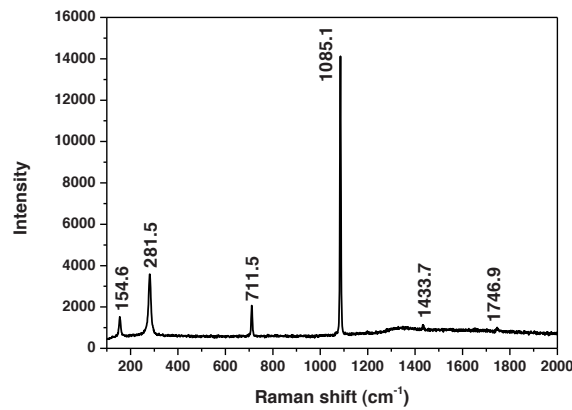


Figure 2.2. Calcite Raman spectrum taken with the Renishaw InVia Reflex confocal Raman spectrometer (for details information on calcite Raman spectrum see chapter five).

The intensity of *Stokes* Raman scattering is:

$$I(\omega_L - \omega_{fi}) = \frac{4\pi(\omega_L - \omega_{fi})^4}{3c^4} I_0(\omega_L) N \sum_{\rho\sigma} (\alpha'_{\rho\sigma})^2 \quad (2.5)$$

where N is the number of scatters, $I_0(\omega_L)$ is the input laser power at frequency ω_L , ω_{fi} is the frequency of the vibrational transition from initial state i to final state f and $\alpha'_{\rho\sigma}$ is the $\rho\sigma$ -component of the polarizability derivative. Normal Raman scattering occurs, when the frequency of the exciting radiation (incident photons) is much less than the frequency of an electronic transition. The normal scattering intensity is proportional to the fourth power of scattered light frequency, $(\omega_L - \omega_{fi})^4$ and it is clear that using excitation sources of higher frequency increase the Raman intensity. Raman intensity increases significantly by moving from near infrared to visible or to ultraviolet exciting source radiations. More details about this subject can be found in the book by Smith and Dent (2005).

2.2.3 Number of normal modes of vibration

A molecular vibration occurs when atoms in a molecule are in a periodic motion. The molecule has a constant translational and rotational motion. The frequency of a periodic motion is known as the vibrational frequency. The number of normal modes of vibration of a molecule with N atoms is determined from the displacements of each atom in the x , y , and z direction. There are $3N$ such displacements, but 3 of these result in a translation of the whole molecule in the x , y , and z direction, and 3 result in molecular rotations. Thus the molecule has $3N-6$ normal modes of vibration. If molecule is linear there are $3N-5$ normal mode vibration, since there is no rotation possible around the molecular axis.

2.2.4 Vibrational dynamics of molecules and solid crystalline

In the simplest approach to calculate molecular vibration modes, a molecule is considered to be isolated. In other words, interactions between molecules and lattice vibrations are ignored. Therefore a normal vibration (no matter how complex) behaves like a harmonic oscillator. For example, a diatomic molecule will have only one normal mode ($3N-5 = 1$), the stretching mode. To keep the centre of gravity in a fixed position both atoms must move in opposite directions. The displacement is inversely proportional to the mass of the atoms.

The molecular vibration modes are described as a function of the force constant (spring coefficient) of the vibration or deformation and the mass of the participating atoms (Fig. 2.3). For this case of vibrating (diatomic species), the vibrational frequency is described by Hook's law:

$$\nu = \frac{1}{2\pi c} \sqrt{\frac{k_0}{\mu}} \quad (2.6)$$

Here μ symbolises the reduced mass of participating atoms ($m_1m_2/(m_1+m_2)$). k_0 is the force constant in Newton per metre. ν is the vibrational frequency in wave numbers. c is the speed of light in centimetres per second. In this model, the interatomic distance, hence the volume and the vibrational frequency are fixed. They do not vary with temperature.

For more complex molecules with more interatomic interaction, different stretching and bending force constants are required. Approximate equations of these force constants and the frequency vibrations for different polyatomic molecules were developed by Herzberg and Nakamoto (Herzberg, 1945; Nakamoto, 1986). They calculated the vibrational modes of different molecular bonds. In their method they measure the vibrational frequency of a complex molecule. However, these calculations were out of the scope of this PhD research project. The objective of this PhD project does not focus on the calculation of the vibrational frequency of different polyatomic molecules in Raman mineral analyses.

According to Hook's law, equation (2.6) the vibrational frequency of a bond is expected to increase with the increasing bond strength and it is expected to decrease with the increasing

mass of the atom involved. For instance, with respect to the bond strength, the stretching frequency increases in the $C - C < C = C < C \equiv C$ sequence (triple bonds are stronger than double bonds, which in turn are stronger than single bonds) and in relation to mass, the vibrational frequency decreases in the $H-F > H-Cl > H-I$ sequence.

There are a number of factors that influence the precise frequency of a molecular vibration; these include:

- The mineral structure and the variety of different compositions in the mineral structure

These effects result in a combination of changes in the Raman peak positions, peak widths and peak intensities. Mineral crystal structures are determined by stoichiometric relationships, relative size of atoms and the nature of molecular bonds. In this PhD research project, Raman spectra are examined to see how frequency shifts when the composition of the mineral changes (see chapter four and five).

- The temperature and pressure factors

Temperature is known to have an influence on Raman scattering frequencies. Depending on the mineral structure, temperature potentially changes the Raman peak position, peak widths, peak intensities and new peaks may appear at low temperatures (~ -90 °C) (Sutherland, 1933; Lucazeau, 2003; Sobron and Wang, 2011).

If the change in temperature causes a change in the molecular structure of the mineral (such as association of simple molecules into more complex aggregates, or a change in the crystalline form of the mineral), then new peaks in the Raman spectrum are expected. Change in temperature could also result in a change of the Raman peak position. Equation 2.6 explains that when temperature decreases, the k_0 (spring coefficient) increases. This also leads to an increase in the vibrational frequency (ν) potentially causing the position of a Raman peak shift to a lower wavelength (ν is correlated to $1/\lambda$). In addition, the peak width refers to the thermal motion (the random motions) of atoms: peak width decreases when temperature decreases. More information on this matter is found in the research by Balkanski and colleagues (Balkanski et al., 1983; Sobron and Wang, 2011).

Pressure and temperature have an effect on a sample's volume and thereby could potentially cause Raman frequency variations. Temperature affects the population of the different vibrational levels ($\nu = 0, 1, \dots$) for each normal mode (Fig. 2.3). The difference between the different energy levels will not be equal and consequently the average position of the atoms will be changed by temperature changes. In both cases (pressure and temperature), the change in the lattice parameters is attributed to the anharmonicity of the potential energy of a molecule (Fig. 2.3). The effects of pressure and temperature on the mineral structures and consequently on the mineral Raman spectra have been discussed in previous studies (Lucazeau, 2003; Mammone and Sharma, 1979; Gillet et al, 1989, 1990, 1993a, 1993c, 1996a, 1997, 2000). However, rare studies exist about the magnitude of the variations of the

Raman shifts under Martian conditions. The study of the Raman shifts variations with temperature and pressure under Martian conditions is important in order to ensure the correct identification of minerals in future missions on Mars. Indeed temperature and pressure are expected to affect the frequency of Raman peaks of mineral on Mars, as temperature and pressure influences the structure of the minerals. However, peak frequencies also vary with mineral composition (such as olivine with different Fo values, see chapter five). Under such situations, then the effects of temperature and pressure have to be precisely quantified if we want to distinguish between the effect of Martian conditions and the effect of different mineral compositions.

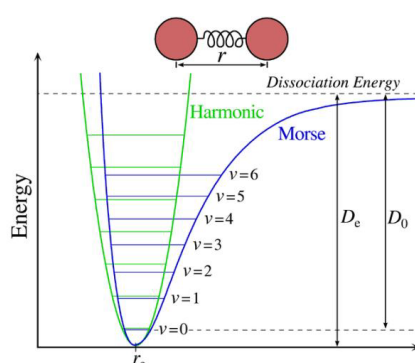


Figure 2.3. The harmonic (green colour) and Morse potential (blue colour) models for the interatomic potential for a diatomic molecule or bond. Morse potential is a model for the potential energy of a diatomic molecule. When describing vibration based on Hook's law, a harmonic oscillator potential is the model. Morse model is described as the deviation of a system from harmonic oscillation or an oscillator not oscillating in simple harmonic motion. r_e is the equilibrium inter nuclear distance (r is intermolecular separation) and D_e is the depth of the potential minimum. Unlike the energy levels of the harmonic oscillator potential (separated by $\hbar\omega$) the Morse potential level spacing decreases as the energy approaches the dissociation energy. The dissociation energy D_e is larger than the true energy needed for dissociation D_0 due to the zero point energy of the lowest ($v = 0$) vibrational level (modified from Reynard, et al., 2012).

2.2.5 Advantages and disadvantages of Raman Spectroscopy

The main benefits of Raman spectroscopy are:

- Non-destructive technique: Raman spectroscopy is a completely non-destructive and non-contact technique. It requires no sample preparation. Raman only involves illuminating a sample with a laser and collecting the scattered photons. Thus it is possible to analyse samples and retain the sample for additional analysis by other techniques such as LIBS if necessary.

- Raman is a technique that distinguishes sample's molecular structures. This technique produces a precise spectral fingerprint, unique to a molecule.
- Fast analytical technique: There is no need to dissolve solid materials, press pellets, dilute samples etc in Raman analysis. Therefore, this analytical technique leads to high quality data in a short period of time. It is potentially a great advantage for space missions.
- Raman is able to be coupled with optical fibre over long distances for remote analysis. Therefore, it is able to work in harsh conditions.

Raman spectroscopy also has certain disadvantages:

- The Raman effect is weak. High power excitation sources are needed to amplify the Raman effect and sensitive detectors are also potentially needed to detect the Raman effect.
- Samples could be destroyed. Raman is usually non-destructive, but if too much laser power is directed at a small point, it can be destructive and burn samples (depends on the selected sample and the laser wavelength). Lowering the laser power significantly reduces the risk of damaging a sample but results in lower signals.
- The interference of fluorescence in Raman spectra. Raman peaks are often swamped or obscured by the background due to fluorescence. Selecting the appropriate excitation wavelength can avoid the fluorescence problem. Choosing an excitation wavelength far from any electronic transitions avoids fluorescence. If the Raman effect is stimulated in the near infrared (NIR) region at a wavelength of 1064 nm, many materials do not show fluorescence. However, the intensity of the Raman scattering depends on the fourth power of the excitation wavelength (see section 2.2.2 Raman intensity). It means that, to avoid the fluorescence effect, the wavelength of the laser excitation should be increased. The intensity of Raman peaks will be weak, however.

2.3 Laser induced breakdown spectroscopy (LIBS)

In this section the basic principle of laser induced breakdown spectroscopy (LIBS) and the advantages and disadvantages of this technique are briefly introduced. The application of this technique under Martian atmospheric conditions is not in the scope of this PhD research study. Nonetheless, studies of LIBS technique under Moon conditions are planned to be evaluated at the VU University in the Martian analogue chamber manufactured as part of this PhD (Colin et al., 2012).

2.3.1 History of LIBS spectroscopy

Laser induced breakdown spectroscopy (LIBS) was first developed as an analytical technique in the 1960's after lasers became commercially available. In the early 1980's there were a few groups working on LIBS. In the past decade the field has expanded greatly with many international groups now investigating and developing a method for a variety of applications. LIBS is also known as a laser-induced plasma spectroscopy (LIPS), laser ablation spectroscopy (LAS), and laser spark spectroscopy (LSS). These terms are rarely used because these abbreviations are often used in other contexts outside the field of optics/spectroscopy. The abbreviation LIBS is the most well-known and is the terminology used in this research project.

LIBS is capable of analysing gases, liquids and solid state materials. It is able to work in harsh conditions (high/low temperature and pressure). In addition, the simplicity and flexibility of the LIBS technique allows it to be applied to a wide variety of substances in material sciences and more recently, in planetary simulation laboratories. Several space missions to bodies in the solar system, such as asteroids, our moon and Jupiter's moon Europa, were equipped with the LIBS instrument. LIBS is capable of providing *in-situ* quantitative elemental analyses of all major and many minor trace elements of planetary surface material.

2.3.2 The basic principles of LIBS

In general terms, LIBS is based on the analysis of the spectral emission from laser-induced sparks or plasmas. Pulsed laser radiation is directed at a small spot (10-200 μm) of sample material. When power densities exceed hundreds of mW/cm^2 , microplasma is formed. The temperature of this plasma is hot, about 10^4 to 10^7 $^\circ\text{C}$. At such a temperature, any material is ablated and ionized (Sergey et al., 1999).

In the early stage of plasma thermalization, electrons interact and recombine with all types of ions so that energy will be released over a broad spectral range from soft X-rays to visible and near infrared (IR). This early plasma stage results in an intense continuous emission. Depending on the power of the laser pulse, the plasma cools down to the point where neutral atoms in excited states are formed, which takes about < 0.1 second.

The most significant parameters for the generation of LIBS plasma are the laser irradiance on the sample and the environmental pressure. On Earth the laser irradiance necessary to generate plasma is above several $10 \text{ mW}/\text{mm}^2$. The plasma expansion is strongly affected by the ambient pressure. According to Knight work, the best pressure condition for LIBS plasma is between 5 and 150 mbar (Knight et al., 2000). This pressure range ensures a modest confinement of the expanding plasma and a moderate rate of ionic and atomic collisions resulting in non-radiative plasma relaxation. This is why the Martian atmosphere (between 6-10 mbar) is suitable for LIBS measurements (Knight et al., 2000; Salle' et al., 2004; Lazic et al., 2007; Rauschenbach et al., 2010). One of the difficulties for interpretation of LIBS data is

that charged ions and molecules that form the plasma can absorb the characteristic wavelengths emitted by elements and the absorption and subsequent re-emission changes the spectral line profile, resulting in broadened lines and a marked increase in the background. This effect is called self-absorption. At very low atmospheric pressure the plasma expansion is fast and self-absorption is minimised. This leads to an advantage for LIBS applications on planetary bodies without or with a very thin atmosphere such as our Moon, Europa (moon of Jupiter) and asteroids (Harris et al., 2005; Pavlov et al., 2011; Lasue et al., 2012).

The spectrum of the plasma contains many peaks that correspond to the optical transitions between particular atomic levels. The LIBS spectrum yields qualitative information about the composition of sample elements. With the proper calibration, quantitative information on the concentration of elements in a sample can also be obtained (e.g., Rauschenbach et al., 2010). LIBS calibration will not be addressed further in this research project. Figure 2.4 presents the LIBS spectral analyses of the Martian basalt (shergottite).

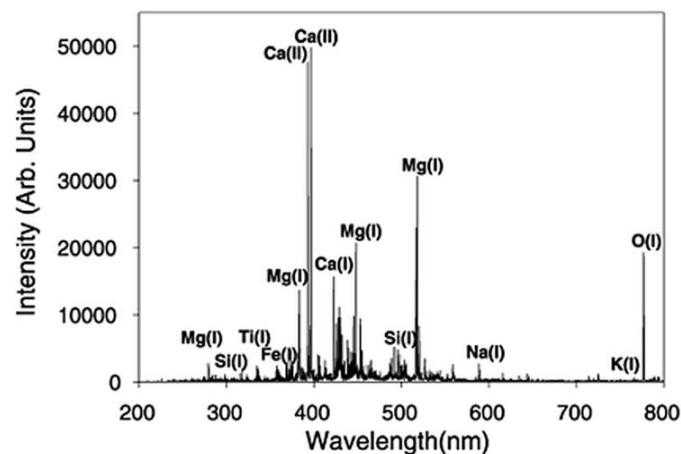


Figure 2.4. Major elemental emission peaks from Dar al Gani 476 (Martian basalt, Shergottite) are labelled in this LIBS spectrum. The Roman numbers in parentheses refer to the ionization state of an atom. (I) is an excited neutral atom; (II) is a singly-ionized atom (from Thompson et al, 2006).

LIBS captures the spectrum of photons emitted by the plasma over the entire 200– 965 nm range over which all elements have emission peaks. To obtain all elements, a large spectral range is essential. Wiens et al. (2005) explained the practical considerations in covering the whole spectral range for LIBS:

- a) Apply a single fixed-grating spectrograph that covers the whole range.
- b) Apply a moveable grating spectrograph, taking successive spectra to cover the whole range of spectral.
- c) Split the light into several fixed-grating spectrographs that together cover the whole range of spectral.

For more details of the advantage and disadvantages of these strategies see Wiens et al. (2005).

2.3.3 Advantages and disadvantages of LIBS spectroscopy

- LIBS is able to analyse a sample directly without the need to prepare the samples beforehand. The LIBS laser radiation may be used for depth profiling and has the effect of cleaning any surface contamination-corrosion. The efficiency of the laser cleaning process depends upon the type of material being removed and the power of the laser.
- The LIBS technique detects all elements from high to low Z such as hydrogen to sodium, which are often not detected by other methodologies. However, LIBS is not applicable when high-sensitivity measurements down to sub-parts per trillion are required. Its field of application lies more in real-time remote sensing without contact with or preparation of the sample.
- In many cases, only one laser pulse is needed to analyse a material. This allows a large number of samples to be identified rapidly. When atomic peaks appear in a spectral region, the chemical composition of a sample is immediately recognized. Thus, it is real time spectroscopy.
- As LIBS is essentially an all-optical technique, only optical access to the material is required to carry out an analysis. This can be achieved by a direct line-of-sight method using a telescope instrument for distances of up to about 10 meters or alternatively with an optical-fibre probe instrument for distances of up to about 100 meters. These features make LIBS a particularly attractive solution for analysis of hazardous or high-temperature materials and for operation in hostile environments, such as space. For example ChemCam on the current Curiosity Rover can take spectra from a distance of about 7 meters (Sallé et al., 2006).

LIBS spectroscopy also has limitations such as:

- Non-reproducibility of the elemental composition detection from the same spot in a sample. Due to the ablation of a sample area, LIBS technology is considered to be a practically non-reproducible technique.

2.4 The RLS instrument

The RLS instrument is composed of three basic parts:

- Two monochromatic laser sources, one each for Raman and for LIBS,
- An optical head (including focussing and collection optics, plus optical fibres),
- A spectrometer,

2.4.1 Laser sources

2.4.1.1 Raman laser source

Exciting radiation for Raman spectroscopy is always provided by lasers. An ideal laser Raman source should emit a stable monochromatic light (UV, Visible, NIR source), with sufficient energy (in general the power of Raman lasers are between a few mW to hundreds of mW) to produce a measurable amount of Raman scattering. The first Raman laser selected for the RLS instrument (designed by Cosine Company with the assistance of Monochrom Company) was a diode laser that weighed less than 30 g, with a ~ 659 nm wavelength and an output power of 20 mW (Fig. 2.5). Using a large sample spot ~ 100 μm with a low laser power (20 mW) avoided the risk of sample damage (Escudero-Sanz et al., 2008). The Raman analyses presented in this PhD research were obtained with the diode laser with a ~ 659 nm wavelength. However, recently the RLS ExoMars team have decided that the diode laser with a wavelength of 659 nm will be replaced with the ~ 532 nm diode laser. Diode lasers have the advantage of being compatible with space missions requirements (small and light, low power, vacuum compatible) and they are now commercially available. The diode laser with 532 nm wavelength was chosen, as it is one of the most used wavelength for Raman spectroscopy.

The choice of the laser wavelength for the RLS instrument was a compromise between increasing the Raman efficiency and limiting the fluorescence. The key aspect when choosing the excitation wavelength is the Raman efficiency. Raman efficiency has an inverse relationship to λ^4 (Rull, 2012). The shorter the laser wavelength, the higher the intensity of the Raman peak will be. However, for short laser wavelengths the fluorescence increases and can obscure the Raman signal by reducing signal to noise, which makes detection of minor peaks more difficult (Harrigan and Goodacre; 2003). For the RLS instrument, the Raman laser excitation has to satisfy the objectives of the ExoMars research (Fig. 2.6). These objectives are:

- a) Investigation of past and/or present life based on the detection of organic compounds and the detection of minerals as indicators of biological activity.
- b) The clarification of water-related processes through the detection of mineral phases produced by fluid-rock interactions.



Figure 2.5. Diode laser, with a mass less than 30 g.

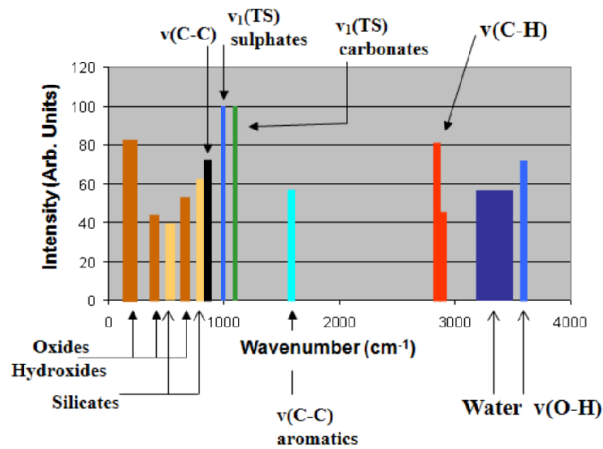


Figure 2.6. Raman spectral ranges for the ExoMars mission.

To produce high quality Raman spectra, the stability of the laser is important. Following delivery of a damaged system to the Vrije University Amsterdam, problems emerged while testing the performance of the 659 nm laser diode that was initially chosen for the RLS instrument. The laser wavelength was found to be unstable over time. This wavelength instability is a characteristic that is often found in diode lasers. The instability resulted in mode hopping, when temperatures changed (McCreery, 2000). To overcome this problem, the original Cosine design for Raman diode laser was coupled with a volume Bragg grating to increase the stability of the laser. However, even with this modification, instability of the Raman laser wavelength was still detected. Close examination of the instability of the laser wavelength showed that the Raman laser wavelength on the RLS instrument is without a doubt too unstable for practical use. Variations in the Raman excitation laser wavelength are shown in Fig. 2.7.

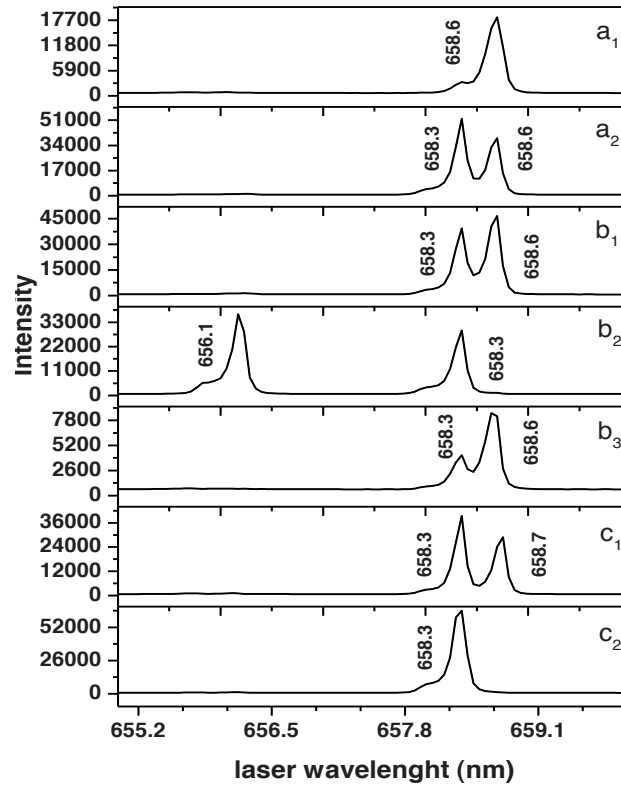


Figure 2.7. Variation in the Raman excitation laser wavelength with: temperatures a₁) 22 °C, a₂) 37 °C, direction of the Raman illumination optical fibre at different angles b₁) 0, b₂) 30, b₃) 45 degrees, c₁) applying stress (by hand) on the Raman illumination optical fibre, c₂) the Raman illumination optical fibre without stress.

Laser wavelength instability was shown to be not only related to temperature change but also with an exact path followed by the light in the Raman illumination optical fibre. The wavelength of Raman excitation laser was different between the edges and core of the optical fibre, (Fig. 2.10). Changes in laser wavelength were also caused by applying stress to the Raman illumination optical fibre. When the instability of the laser wavelength was proved, detailed step by step analyses of the causes of this instability were considered. The goal was to find practical solutions to overcome to the laser instability.

The following solutions were evaluated to minimise the effect of the ambient temperature:

- i) lab temperature control

In an attempt to overcome some of the wavelength instability, a first approach was made to insulate the laser diode with thermoplastic elastomeric foam of 20 mm thickness in the

laminar flow cabin. Nevertheless, the laser wavelength remained unstable. The record of the ambient temperature in the lab and flow cabin where the laser was operated shows over 3.5 degree variations with ~ 4 hours intervals (Fig. 2.8, a). The air conditioning was designed to provide a temperature stability of ± 1 °C per hour. Examination of the design showed that the system was cooling too vigorously and it had a poor thermal regulation. After extensive testing and several consultations with the service company the implemented solution was to reduce the amount of water to the heat exchanger and to permanently activate the circulation fan that would then circulate on low power. This helped maintaining lab temperature to within ± 1 °C of the desired value. The optimal temperature range to provide a stable wavelength is between 16 and 24 °C, based on studies by Cosine and Monocrom (Fig. 2.8, b). Temperatures higher than 24 °C are expected to cause laser instability and a significant change in laser wavelength. Therefore, lab temperature was fixed at 20 °C. All in all, the Raman laser wavelength was still unstable.

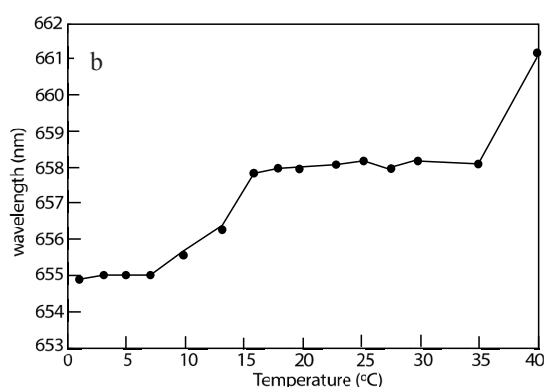
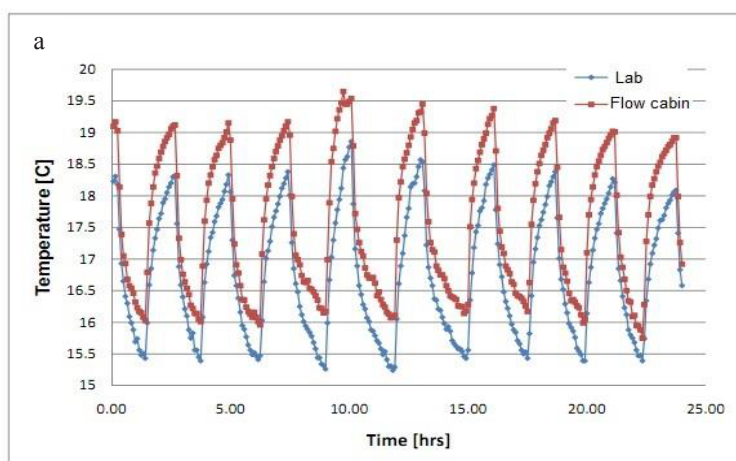


Figure 2.8. a) Temperature variation in the lab and flow cabin over one day prior to the renovation of the air conditioning system. Instability in temperature resulted in laser wavelength instability, b) Output wavelength of the Raman laser package as a function of temperature. The measurements were performed at the Monocrom Company in Spain.

ii) laser diode with heat sink

The ambient temperature around the Raman laser diode and the temperature of the laser diode were monitored with two handheld thermocouples. This showed a 5 degree difference between ambient temperature and local temperature of the Raman laser diode. The power of the Raman laser diode (20 mW) was sufficient to raise the local temperature in the device's environment. This could potentially lead to an unstable wavelength. To improve the cooling of the diode, an aluminium block was added to act as a thermal sink. This block had a size of 100 x 80 x 30 mm. The aluminium block was screwed to the gold-plated copper block at the base of the Raman laser diode (Fig. 2.9).

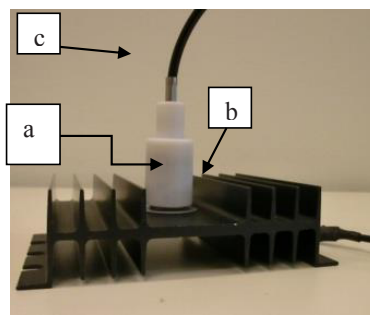


Figure 2.9. a) Raman laser diode attached from one side to b) aluminium heat sink and c) the Raman illumination optical fibre.

This aluminium thermal block was designed to have a large surface area (see Fig 2.9) and a consequently better thermal cooling capacity. As a result, the Raman laser diode could exchange heat more efficient with its environment and the Raman laser wavelength could be stable.

Finally to overcome the potential instability of the laser wavelength caused by changes in the stress on the optical fibre, the optical fibre was placed in a fixed position, carefully handled and protected to prevent the laser instability.

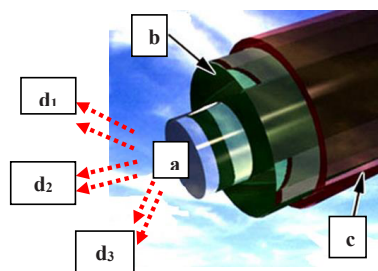


Figure 2.10. An optical fibre consists of: a) Core: The core of a conventional optical fibre is a cylinder of glass or plastic that runs along the fibre's length. b) Cladding: a medium with a lower index of refraction, which surrounds the core, c) Buffer: Protects cladding from moisture and physical damage. Raman laser excitation beam may have different wavelengths (d_1 , d_2 , d_3) in the centre and on the edges of the core in the Raman illumination optical fibre.

Raman spectra were only obtained when room temperature was around 20 °C, the Raman illumination optical fibre was fixed and there were no pressure on it. These actions improved the laser stability but the current design means that the RLS remains highly sensitive to very minor changes in the local environment and is impractical for use as a portable instrument.

2.4.1.2 LIBS laser source

The selected laser source for the LIBS system in the RLS instrument was a neodymium-doped yttrium aluminium garnet (Nd:YAG) solid state laser with 1064 nm wavelength. This laser is a reliable and convenient source for powerful pulse generation needed to produce a plasma under Martian conditions (Escudero-Sanz et al., 2008).

2.4.2 Optical head

As a final stage in the design of the RLS instrument a functional optical head was designed and manufactured by TNO. This optical head has a diameter of 300 mm and height of 300 mm (Fig. 2.11). The optical head included lenses (to parallelise and to focus light), parabolic metal mirrors to reflect light, optical fibres for light transfer and filters for Raman spectroscopy (a notch filter and a band-pass filter).

The first objective of the optical head was to direct laser light from either the Raman or LIBS laser to a sample to create Raman scattering or a plasma. The second objective was to catch Raman scattering or light from the plasma and direct it to the RLS spectrometer. Therefore, the optical head has effectively two sample illumination channels and two optical viewing channels linked to respectively the LIBS/Raman lasers (Fig. 2.11). To obtain sensitive detection levels, efficient light transmission is required across a wide spectral range. The required transmission spectral ranges are given in Table 2.1.

Channel no.	Channel description	Spectral range (nm)
1	Raman viewing	669 to 840
2	Raman illumination	659
3	LIBS viewing	240 to 840
4	LIBS illumination	1064

Table 2.1. Spectral coverage required for the optical head.

When laser light is directed at the sample with an optical fibre, it is critical to remove the Raman peaks and fluorescence that are excited in the optical fibre by the laser. Band pass filters are designed to transmit light with a limited range of wavelengths, typically 1– 10 nm. This is an effective way to ensure that the lasers light is not contaminated by secondary

wavelengths inherited from optical fibres, mirrors, prisms etc. Notch filters are used in the opposite way to suppress the laser wavelength; i.e., Rayleigh scattered light derived from the laser light. The use of the notch filter is vital since the Raman effect is very weak (Escudero-Sanz et al., 2008).

In the sketch of the optical head, Fig. 2.11, the optical paths in red colour indicate the direction of the Raman excitation laser light to a sample and the direction of Raman emission from sample to the spectrometer (Fig. 2.11). In detailed the optical path is as follows:

- a) The Raman laser light is first parallelised by a convex lens at the output of the Raman illumination optical fibre.
- b) The Raman laser light is filtered by a band pass filter.
- c) The parallel Raman laser light is reflected from a notch filter to a mirror.
- d) The reflected Raman laser light is focussed onto a sample surface via a convex lens.
- e) The Raman scattered light generated by the sample is parallelised by a convex lens.
- f) The Raman emission light is reflected by a mirror to the notch filter where the Raman emission is transmitted through the notch filter while the elastically scattered light is blocked by the notch filter.
- g) The light is focussed into an optical fibre via a convex lens and continues to the spectrometer.

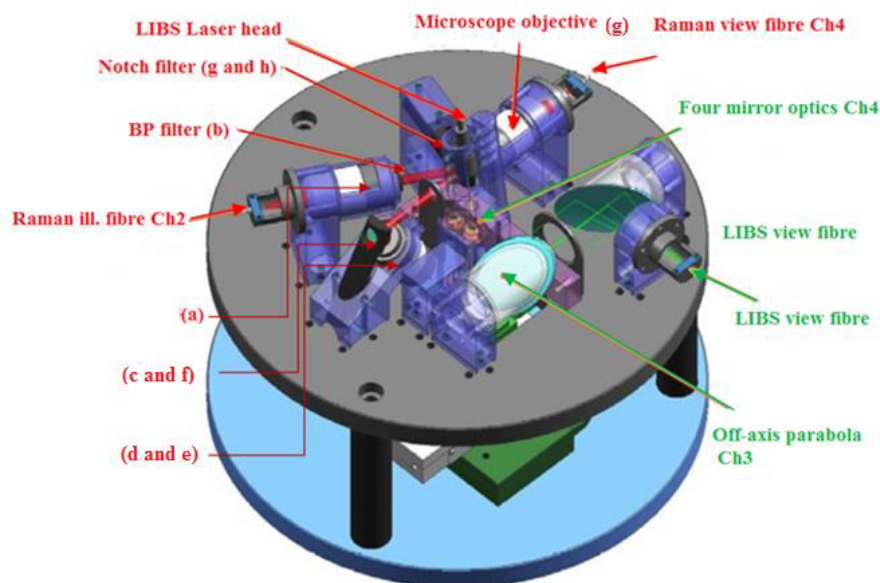


Figure 2.11. The mechanical design of the optical head. The optical head consists of four different optical channels/pathways for illumination and detection. The optical head collects Raman scattered light (red optical paths) and light from the plasma (green optical path). There are two illumination and two detection channels for both Raman and LIBS techniques. (Abbreviation of “ill” refers to illumination).

In Fig 2.11 the paths in green colour indicate the direction of the LIBS laser light to a sample and the light of the plasma to the spectrometer. The LIBS laser light is first reflected from

several mirrors and then arrives at a sample. When the light from plasma is emitted in all directions, a concave lens focuses a portion of the light emitted from the plasma to a convex mirror. Finally, the light from plasma is reflected by several flat and convex mirrors to reach the LIBS viewing optical fibre and thereby on to the spectrometer.

Due to the LIBS technique producing a plasma, it is vital that the optics are protected from the deposition of ablated sample material. Therefore, the sample is maintained at a minimum distance of 50 mm from the optics to reduce as much as possible fouling of the optics.

2.4.3 Spectrometer

The most challenging requirement in the design of RLS instrument was maintaining a small volume and low mass that was robust enough to be capable of operating under Martian conditions (Fig. 2.12). The RLS spectrometer is compact (190 x 150 x 190 mm) and weighs less than 850 g (Cour`eges-Lacoste et al., 2007). It contains the prism, grating, lenses, mirrors and a CCD detector.

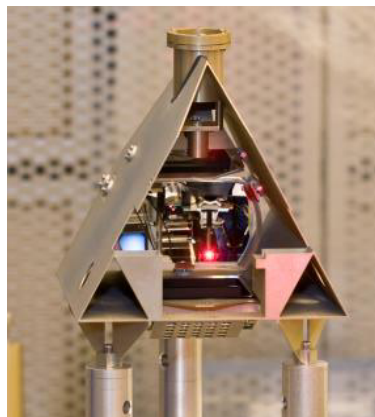


Figure 2.12. The RLS spectrometer is compact (190 x 150 x 190 mm).

The RLS spectrometer uses a prism to disperse the light. Dispersion is the phenomenon by which a spectrum of light is separated vertically by wavelengths. The dispersion of light reaches a grating where it diffracts light into several waves travelling in different directions. Figure 2.13 (a) shows the easiest method to explain the function of a reflection grating. This figure shows a light ray of wavelength λ incident at an angle α and diffracted by a grating (of groove spacing d) along angles β_m . These angles are measured relative to the “grating normal” (Fig. 2.13a), which is the plane perpendicular to the grating surface at its centre (dashed line in the figure). In a reflection grating, the angles $\alpha > 0$ and $\beta_1 > 0$ (as they are measured counterclockwise from the grating normal) whereas the angles $\beta_0 < 0$ and $\beta_{-1} < 0$ as they are measured clockwise from the grating normal (Fig 2.13a). Another figure of grating diffraction, using wavefronts (surfaces of constant phase), is shown in Fig. 2.13 (b). The geometrical path difference between light from adjacent grooves is $d \sin\alpha + d \sin\beta$. (Since β

< 0 , the latter term is actually negative). If this difference equals the wavelength λ of the light (or some multiple integral thereof), the light from adjacent grooves will be in phase (leading to constructive interference). At all other angles of β , there will be some measure of destructive interference between the wavelets originating from the groove surfaces. These relations are shown by the grating equation $m\lambda = d(\sin\alpha + \sin\beta)$. Here m is the diffraction order, which is an integer.

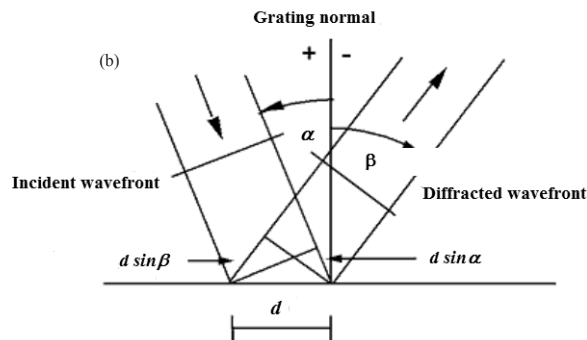
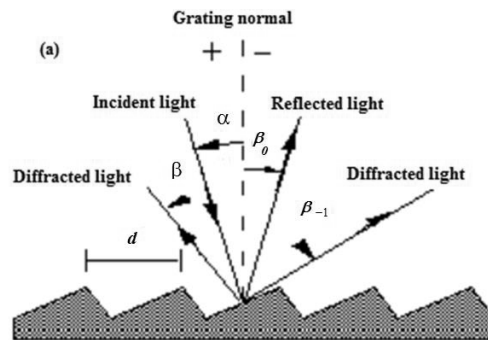


Figure 2.13. a) Diffraction by a plane grating. A beam of monochromatic light of wavelength λ is incident on a grating and diffracted along several discrete paths, b) Geometry of diffraction, for planar wavefronts (modified after <http://gratings.newport.com/library/handbook/chapter2.asp>).

In RLS instrument, Raman peaks appear in the third order, from 660 to 840 nm. The LIBS signals appear on the orders in the region from 240 to 630 nm. Table 2.2 shows the specific ranges of each order.

Diffraction order	Wavelength range on detector (nm)
1	1950 to 2520 (CCD not sensitive)
2	975 to 1260 (CCD sensitive to 1100, visibility of LIBS laser)
3	650 to 840 (Raman shift detection)
4	504 to 630
5	406 to 504
6	345 to 406
7	300 to 345
8	265 to 300
9	240 to 265
10	195 to 252
11	177 to 229

Table 2.2. Wavelength ranges of diffraction orders as shown on the detector.

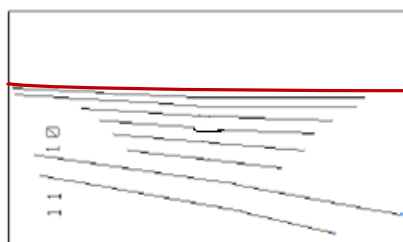


Figure 2.14. Diffraction orders imaged on the detector, the 3th order is shown in red colour and 10th and 11th are the last orders from bottom.

Detector

A charge-coupled device (CCD) is used to transform light (Raman scattered light or the light from the plasma) into an electrical signal. The selected CCD for RLS instrument is a back-illuminated device with 2048 x 2048 pixels that are 13.5 μm square (Fig. 2.15). The CCD has a UV coating in order to increase the quantum efficiency (QE) in UV region. The quantum efficiency is the percentage of photons hitting the CCD surface.

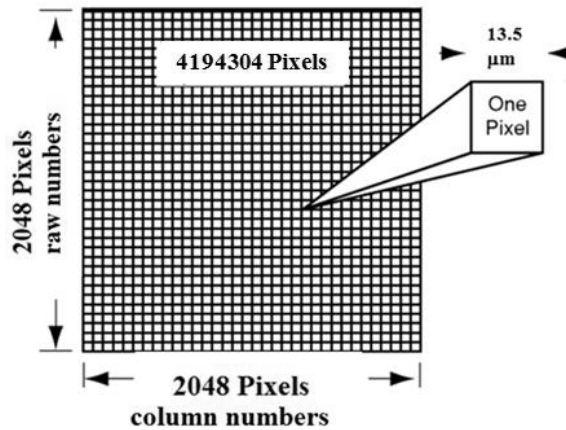


Figure 2.15. The basic design of a charge-coupled device (CCD) detector.

Minimisation of noise is one of the most important qualities required for a detector. Noise is an unwanted signal, either present in the relevant light signal or produced by the imaging process. It leads to inaccurate measurements of the light signal distribution (image). Noise usually comes from three main sources:

- a) Photon or shot noise: The random arrival of photons on a CCD cause shot noise. Since each photon is an independent event, the arrival of any given photon cannot be accurately predicted. Instead the probability of its arrival in a given time period is described by a Poisson distribution. Shot noise can be reduced by obtaining spectra with longer acquisition times effectively averaging out the random noise or by combining multiple frames again averaging the background.
- b) Thermal noise (dark noise): Additional electrons are generated within the CCD not by the absorption of photons (signal) but by physical processes within the CCD itself. The number of electrons generated per second by the CCD itself will depend on the operating temperature of the CCD. This noise is known as thermal noise (dark noise). The amount of dark noise decreases by a factor of two for every 7 or 8 °C drop in temperature (Denson et al., 2007). CCDs are cooled by either Peltier systems down to -100 °C (it is common to be -70 °C) or by liquid nitrogen down to -140 °C.
- c) The CCD reads each pixel through an amplifier. Noise is also generated during the conversion of the electric charge into a voltage signal. This noise increases proportionally with the number of readings.

Consequently to obtain the best possible results the CCD temperature of the RLS instrument had to be as low as possible to reduce thermal noise. A cooling system was designed, developed and tested during this research process to help reduce thermal noise. Details of the water cooled Peltier system are discussed in chapter three.

The CCD was connected to an electronic box. The electronic box provided the bias voltages and timing signals required to operate the CCD. The raw CCD images were taken using

dedicated software written by colleagues from the University of Leicester (such as a raw image in Fig 2.18) and they were stored on a dedicated PC. The raw CCD images were then processed by in-house software (programmed by Dr. Aurelia Colin, Vrije University Amsterdam) to produce data such as Raman wavelength shifts and their intensities. Finally, Raman spectra were processed and spectra were obtained via the Origin program. The identification of the peak positions in the Origin program was done using Gaussian fitting, Fig. 2.16.

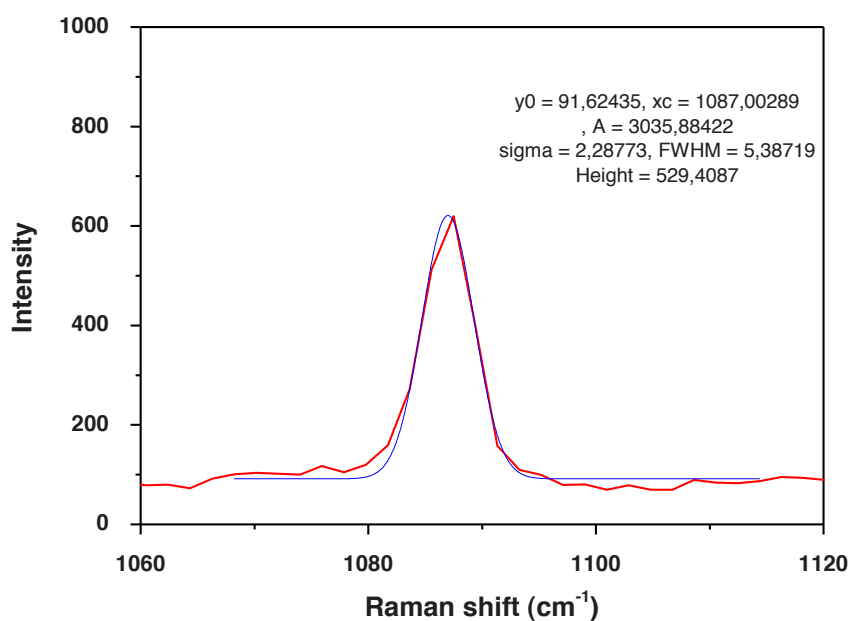


Figure 2.16. RLS calcite Raman spectrum, peak at 1087 cm^{-1} was determined using Gaussian fitting with Origin program. For each Gaussian peak, the parameter table shows y_0 , x_c , A and w , which means: y_0 is base, x_c is the position of the centre of the peak, A is area and FWHM is full width at half maximum.

Figure 2.17 shows an example of a peak fitted with a Gaussian function:

$$y = y_0 + \frac{Ae^{-\frac{4\ln(2)(x-x_c)^2}{w^2}}}{w\sqrt{\frac{\pi}{4\ln(2)}}} \quad (2.7)$$

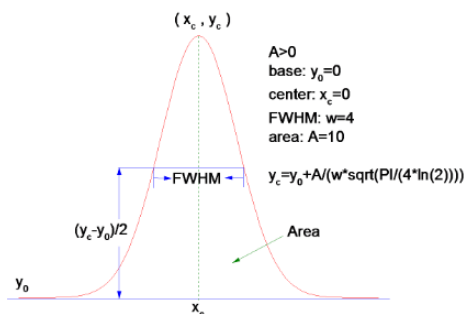


Figure 2.17. An example of a calculated peak using the Gaussian function. For each Gaussian peak, the parameter table shows y_0 , x_c , A and w , where: y_0 is base, x_c is the position of the centre of the peak, A is area and w is FWHM.

2.5 Characteristics of the RLS instrument

As the RLS instrument is designed to operate under Martian conditions, the stability of the instrument needed to be validated at various temperatures. Consequently, a series of experiments were carried out at different temperatures to determine the performance of the RLS spectrometer.

2.5.1 Instrument resolution

One of the most important characteristic of a spectrometer is the spectral resolution. The spectral resolution of the spectrometer provides the ability to separate two peaks. It resolves two non-coherent radiations with the same intensity and full width at half maximum (FWHM), at λ and $\lambda + \Delta \lambda$ respectively, when the distance between their centres are equal or greater than their FWHM. The resolution of a spectrometer depends on the number of grooves in the grating, focal length of the spectrometer, size of the individual pixels in the CCD, size of the slit and the light wavelength. The spectral resolution is usually determined by measuring the FWHM of an emission line of a calibration lamp.

The spectral resolution of the RLS spectrometer was determined by measuring the FWHM of an emission peak of a mercury lamp. A mercury lamp was used to illuminate the spectrometer. One of the sharp peaks of the mercury spectrum was selected for calculating the FWHM.

The Origin program, which analyse the peaks of the RLS Raman spectra, was used to calculate the FWHM of the sharp peak of the mercury spectrum. The Gaussian function was selected in the Origin programme to fit a Gaussian to the intensive peak of mercury lamp and then calculate the FWHM of the fitted peak.

The spectral resolution was determined to be $\sim 0.2 \text{ nm}$ ($\sim 4 \text{ cm}^{-1}$). When the resolution of RLS instrument is 0.2 nm , it means that RLS instrument is capable of distinguishing adjacent Raman peaks separated by more than 0.2 nm .

2.5.2 Calibration of the CCD at different temperatures

To determine if the spectrometer will function under variable Martian conditions where daily temperatures may vary by several tens of degrees a major effort was spent in determining if Raman spectrum drifts with temperature. In this section the calibration procedure for the 3rd order is described in detail. This is where Raman Stokes vibration modes are detected with respect to the $\sim 659 \text{ nm}$ red excitation laser light. The calibration was performed in two steps:

- First the position of the different orders on the CCD is determined
- Second, for each order a correspondence between the column number of the pixels in the CCD image and the associated wavelength is determined.

2.5.2.1 White light to determine position of the third order

White light is the combination of all the colours of the visible light spectrum and includes the wavelength of the 3rd order (from 640 to 840 nm). Therefore, the RLS instrument was illuminated with white light in order to determine the position of the 3rd order in the CCD image. Figure 2.18 is an image of the CCD illuminated by white light. In the figures a series of light gray spots (pixels) create lines to form the different diffracted orders.

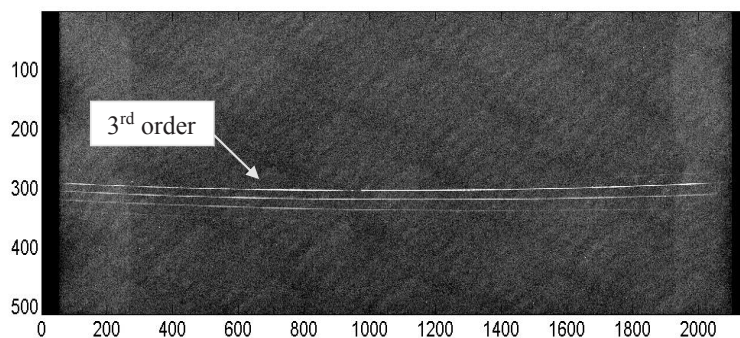


Figure 2.18. An image of the CCD, illuminated by white light. The almost complete orders that are visible in this image are the 3rd, 4th and the 5th orders with part of the second order visible on the right and sixth order on the left.

An in-house software programme was built to evaluate the CCD output (Dr. Aurelia Colin, Vrije University Amsterdam). This programme modelled the position of the orders and gave the user the ability to choose selected pixels on the CCD image to define a specific order.

The software records the position of these pixels (X is the column number of the CCD; Y is the row number of the CCD). In Fig. 2.19 the third order is shown. After the initial selection of pixels the software makes a polynomial regression fit to the data to define the 3rd order. At this stage the user zooms in on the image and refines the selected data points to optimise the curve fitting.

The software averages the light level of an individual pixels by including pixels above and below in the Y direction. Therefore, if there was a shift in the calibration in the Y direction of one pixel or less it would not affect the position of the final calibration spectrum. The user can check the accuracy of the fit and if required make manual adjustment to optimise the fit. The position of the line is reproducible to less than one pixel of difference over the period of the study at a specific temperature.

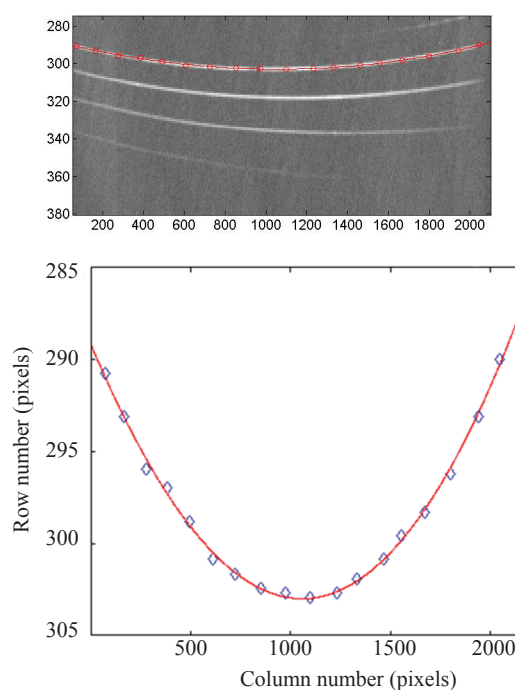


Figure 2.19. A 3rd order polynomial fit for the 3rd order of the spectrum over the wavelength 640 to 840 nm.

Figure 2.20 illustrates the position of the 3rd order on the CCD at 10, -5 and -20 °C. The position of these smoothed curves shifted along the vertical axes depending on the temperature of the RLS instrument. Significantly there was no resolvable variation of wavelength along the X axis. The total change in the Y axis was ~ 3 pixels ($40 \mu\text{m}$) over the 30 °C range. Note that the temperature of the CCD itself was kept between ~ -30 and -40 °C (depending on the temperature of the analytical chamber). Studies that involved varying the temperature of the CCD did not influence the position of the 3rd order. We therefore ascribe the shift in the Y axis in Fig. 2.20 to changing performance of the optics in the spectrometer,

most likely the prism, which diffracts the light in Y direction in the RLS spectrometer. The optical properties of the prism made of glass potentially depended on temperature. In addition, despite the design considerations and robust manufacture the position of the prism and its distance from CCD could change due to thermal contraction associated with lower temperatures. We recommend that the instrument designers (TNO) conduct a more thorough thermal analysis of the spectrometer to ascertain in detail the origin of the minor temperature induced spectral offsets so that designs of spectrometers for future missions that may be subjected to more extreme temperature conditions can be optimised. In conclusion, although the prism in the RLS instrument appears to cause minor variations in the position of the spectrum under varying thermal conditions, the offset is only in the Y direction and consequently does not affect calibrations of Raman spectra. As such the instrument is functional for the study of minerals under Martian conditions.

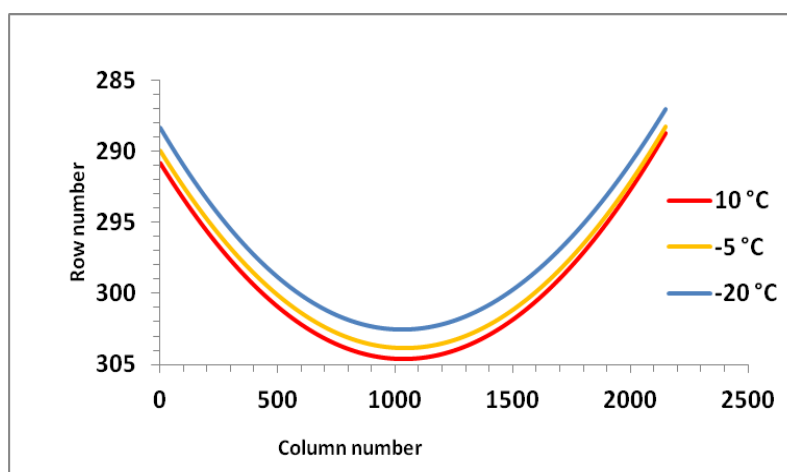


Figure 2.20. The position of the 3rd order on the CCD at 10, 5 and -20 °C.

2.5.2.2 *Calibration of the CCD column number to wavelength*

When the position of the 3rd order had been set for each temperature, the spectrum was calibrated for wavelength (X direction on the CCD). For this step, argon and neon lamps were used. These lamps produce narrow, intense peaks between 660 and 840 nm with known wavelengths.

Using the in-house software, the calibration peaks were identified and fitted individually using the Gaussian function, thereby determining the centre of the peak. The software allowed the user to ascribe the column number of the centre of the different peaks to known

wavelengths from the literature. The software calculated a 3rd order polynomial adjustment to fit wavelength as a function of the column number. In case of mistakes in ascribing peaks, the user had the possibility to modify the calibration or to add more peaks with another lamp. An example of a calibration adjustment is shown Fig. 2.21. As discussed above the calibration procedure showed variation with temperature but only in the Y direction. Column numbers were always within error, irrespective of temperature (the difference between theoretical fit value and calibration lamp value) (Fig. 2.22). This means that the position of the peaks only shifts significantly in the Y direction. Figure 2.22b establishes that the differences between the calibrations at different temperatures are always less than 0.2 nm. However, on average there is a positive offset of ~ 0.1 nm for the -20 °C data. This difference is within our resolution capabilities but suggests that if the CCD is operated at even lower temperatures a specific calibration may be required.

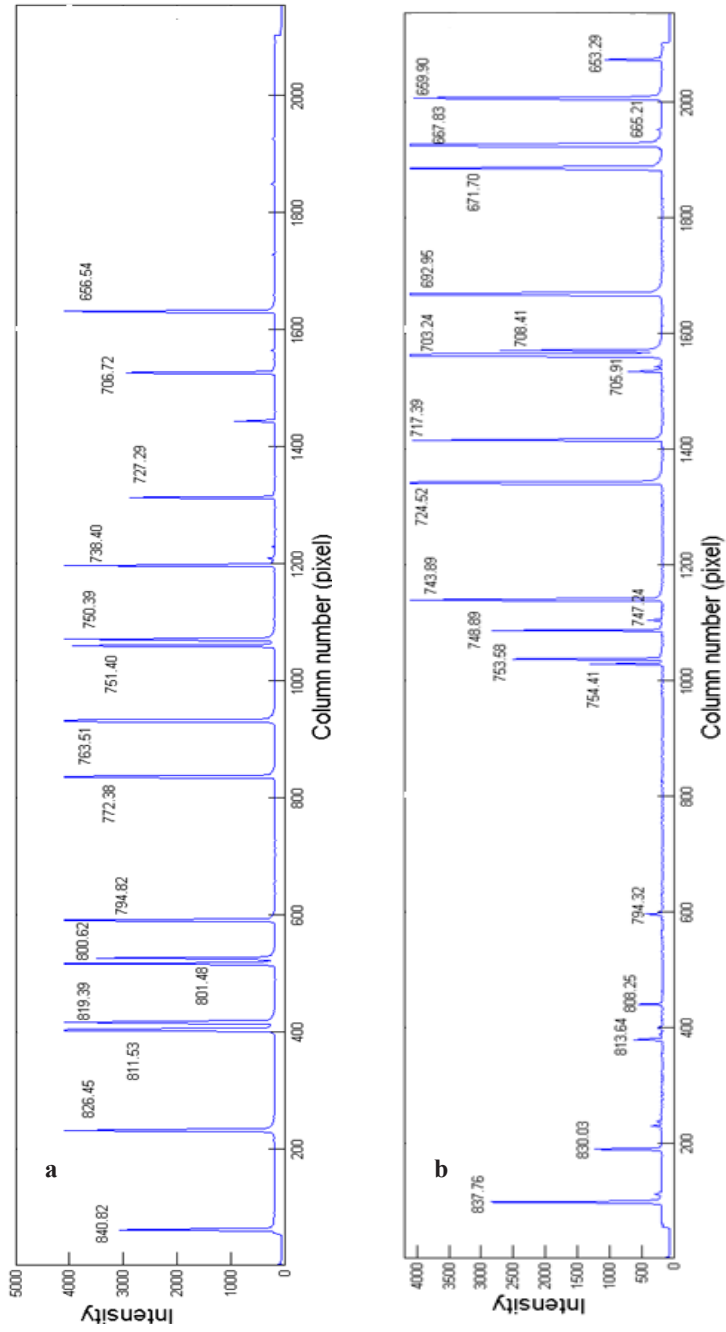


Figure 2.21. RLS spectra of a) argon, b) neon calibration lamps and peak wavelength of the identified peaks from the literature.

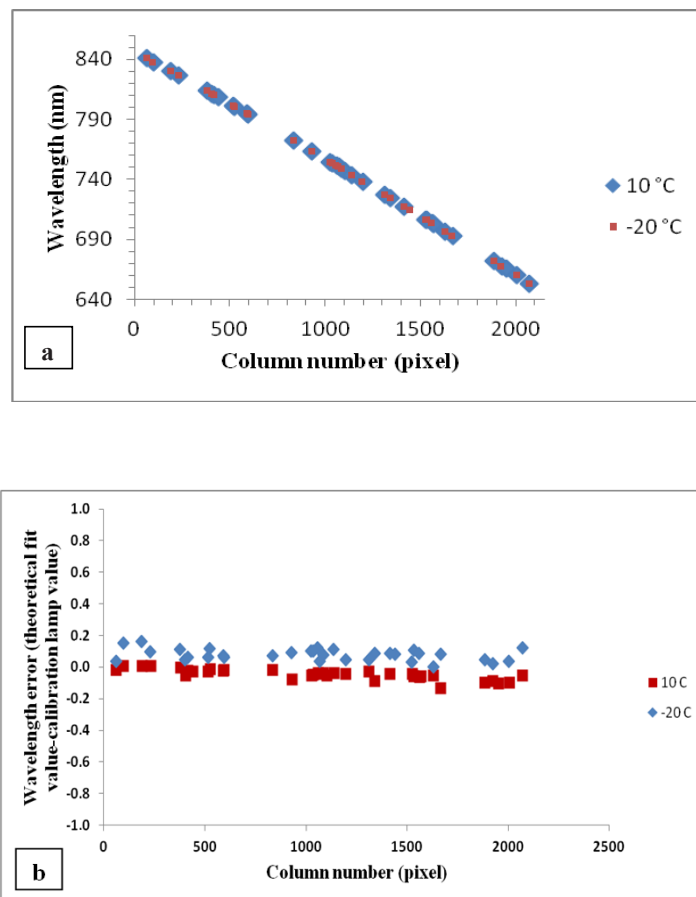


Figure 2.22. a) CCD column plotted against wavelength at 10 and -20 °C, note there is no significant change in the calibration with temperature, b) CCD column plotted against difference from theoretical fit of the curve. The difference between the calibrations is always less than 0.2 nm.

2.5.2.3 Accuracy of Raman shift values

The observed error of the CCD calibration is presented in Table 2.3.

The errors were calculated based on the difference between literature values (literature values after Newport company: <http://www.newport.com/Pencil-Style-Calibration-Lamps/377846/1033/info.aspx>) and the value calculated from the calibration. The root-mean-square error (RMSE) of the individual errors associated with the calibration lamp peaks was calculated. An error of ~ 0.02 nm or 0.4 cm^{-1} was obtained.

Wavelength literature (nm)	Wavelength calculated from calibration (nm)	Difference (nm)
840.82	840.81	-0.01
826.45	826.46	0.01
811.53	811.50	-0.03
810.37	810.37	0.00
801.48	801.48	0.00
800.62	800.63	0.01
794.82	794.82	0.00
772.38	772.40	0.02
763.51	763.47	-0.04
751.46	751.47	0.01
750.39	750.39	0.00
738.4	738.41	0.01
727.29	727.32	0.03
706.72	706.74	0.02
696.54	696.56	0.02
837.76	837.77	0.01
830.03	830.04	0.01
813.64	813.65	0.01
808.25	808.24	-0.01
794.32	794.33	0.01
754.41	754.40	-0.01
753.58	753.58	0.00
748.89	748.90	0.01
747.24	747.23	-0.01
743.89	743.90	0.01

724.52	724.49	-0.03
717.39	717.41	0.02
705.91	705.92	0.01
703.24	703.24	0.00
702.41	702.42	0.01
692.95	692.89	-0.06
671.7	671.68	-0.02
667.83	667.83	0.00
665.21	665.19	-0.02
659.9	659.89	-0.01
653.29	653.33	0.04
Root-mean-square error		0.02 nm

Table 2.3. The observed error of the CCD calibration procedure.

To assess the realistic level of error during Raman analysis multiple analyses were undertaken. This was initially carried out on a commercial Renishaw InVia Reflex confocal Raman microscope. This commercial spectroscope uses a 785 nm diode laser as excitation source. The spectral resolution of adjacent peaks in the system is $\sim 3 \text{ cm}^{-1}$ and the accuracy of the system is about 0.1 cm^{-1} (according to the specifications provided by Renishaw). Fig 2.2 is an example of a calcite Raman spectrum taken via Renishaw InVia Reflex confocal Raman microscope.

The Raman spectrum of a calcite sample was determined ten times over a period of a day to calculate the standard deviation in the Renishaw measurements, Table 2.4. Raman peak positions determined for the 1086 cm^{-1} , has a standard deviation of 0.04 cm^{-1} using the Origin program to fit the peaks (Gaussian).

Analysis number	Wavelength (cm⁻¹)
Measurement 1	1086.29
Measurement 2	1086.25
Measurement 3	1086.24
Measurement 4	1086.25
Measurement 5	1086.29
Measurement 6	1086.37
Measurement 7	1086.34
Measurement 8	1086.33
Measurement 9	1086.34
Measurement 10	1086.29
Average	1086.30
2Sigma	0.08

Table 2.4. The Renishaw Raman calcite peak determined ten times on the same spot over a period of a day to calculate the error in the Renishaw measurements.

The same method was subsequently applied to a calcite sample using the RLS instrument. The measurements show that the software can fit the data within an error of ~ 0.02 nm or 0.5 cm⁻¹, Table 2.5. However, we consider this an unrepresentative experiment of the instrument capability due to the instability of the laser. The data in table 2.5 represents the best data from ~ 25 analyses that show the smallest variation in laser wavelength.

Analysis number	Wavelength (cm⁻¹)
Measurement 1	1087.00
Measurement 2	1087.21
Measurement 3	1086.80
Measurement 4	1087.01
Measurement 5	1087.10
Measurement 6	1087.00
Measurement 7	1087.34
Measurement 8	1087.60
Average	1087.14
2Sigma	0.48

Table 2.5. The RLS Raman calcite peak (on a same spot) was determined eight times over a period of a day to calculate the error in the RLS measurements.

This accuracy is four times worse than the commercial Renishaw InVia Reflex confocal Raman microscope. However, based on the determination of the calibration lamps we are certain that with a stable laser the accuracy of the system would be better than 0.4 cm⁻¹. For the application of Mars missions this accuracy is suitable to achieve the main objectives we listed in chapter 1. For instance, it is enough to distinguish between calcite and aragonite ν_4 asymmetric bending vibration mode at 711.5 and 703.5 cm⁻¹ respectively.

2.5.3 CCD noise and the detection limit of Raman signals

In addition to the reproducibility of the instrument, an important aspect of the practical operation of the RLS instrument is the ability to detect and fit Raman peaks to the measured data. Above we examined the ability to fit large Raman peaks with reproducibility. An additional important question is the ability of the methodology to detect individual low amplitude Raman peaks. In this respect the signal to noise ratio is a key aspect.

Signal to noise ratio (SNR) is a measure of signal strength relative to background noise. Noise is the unwanted electrical or electromagnetic energy that is detected within the instrument and potentially degrades the quality of peaks. The signal to noise ratio will vary mainly dependent on the thermal design of the instrument and also the ambient thermal conditions. Commonly agreed threshold suggests that SNR lower than 3 makes Raman peaks hard to detect. Hence the operational temperature of the CCD is a key aspect of how well instrument functions.

$$\frac{S}{N} = \frac{\text{Mean}}{\text{Noise}} = \frac{\bar{x}}{\sigma} \quad (2.8)$$

Under Martian conditions temperature fluctuations will affect the noise level in Raman spectra. Therefore noise (σ) was calculated at two different temperatures (-30 and -40 °C). σ is equal to the standard deviation of the baseline noise intensity in the random region divided by $\sqrt{2}$.

$$\sigma = \text{STDEV} / \sqrt{2} \quad (2.9)$$

When operating the CCD at temperatures \sim -30 and -40 °C, noise values were \sim 5 and 3 respectively (Figs. 2.23 and 2.24). This means that, when the CCD is operated at \sim -40 °C, the peak detection limit is about two times better than the peak detection limit of CCD operated at -30 °C.

Due to the direct temperature dependency of CCD noise, the spectrometer does not operate at high efficiency when the CCD temperature is higher than -30 °C. With the presence of CO₂ at 8 and -8 °C inside the experimental chamber, the CCD could not reach -30 °C (respectively -17 and -25 °C, cf. chapter 3). These conditions are a limitation to the study of the influence of Martian conditions on small peaks in individual Raman spectra. In the following chapters, under CO₂ atmosphere, only data obtained with the atmosphere at -20 °C are presented, i.e., when CCD temperature reaches -34 °C.

Previous theoretical studies have emphasised that operating CCD at the lowest possible temperature improves signal to noise ratio (Chadwick and Cooper, 2012) and our practical experiences emphasises this conclusion. Given the outcome of measurements reported later in the thesis (Chapters four and five) stresses that it is not always possible to obtain strong Raman signals from minerals and that under the practical operational conditions on the

surface of Mars SNR optimisation will be important. Ensuring efficient insulation and cooling of the CCD in the RLS instrument on ExoMars mission is a vital design requirement.

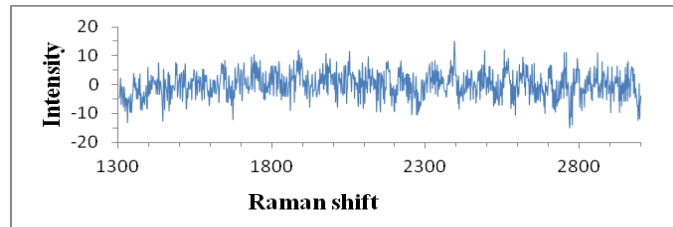


Figure 2.23. When CCD was operated at ~ -40 °C, noise was about 3.

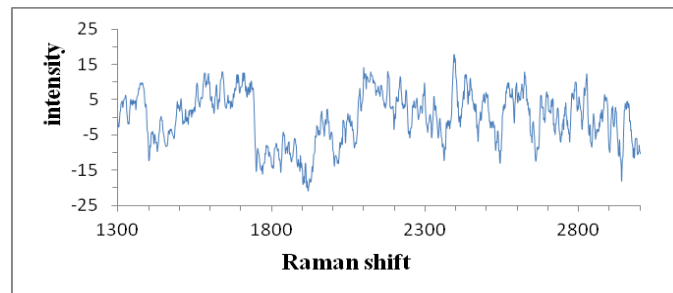


Figure 2.24. When CCD was operated at ~ -30 °C, noise was about 5.

2.6 Conclusion

In this chapter, the optical design of the RLS instrument (designed to work under Martian conditions) was compared to the design specifications from TNO. The instrument was intended to become the basis for realizing the instrument flight model for the ESA's ExoMars mission. The RLS instrument is shown to be capable of working under challenging environment conditions such as Mars conditions (8 mbar CO₂ and +10 to -20 °C). The instrument survived repeated cycling of the instrument between ambient terrestrial conditions and Martian conditions without long term changes in the calibration curves of the instrument.

Calibration of the CCD detector at different temperatures showed that the RLS instrument undergoes minor changes. Although, this effect did not change the horizontal position of Raman peaks (wavenumbers), it should be taken into account for the design of the RLS flight mode. Based on the design of the spectrometer we believe that the thermal characteristics of the prism or expansion-contraction of components that effectively change the position of the prism relative to other optical components.

It was established that the largest error in the determination of peak wavelengths during Raman analyses was 0.4 cm^{-1} . The SNR is a vital aspect of the instrument design and more efforts need to be made in optimising the system. The ability to extract mineral structure information with the RLS instrument is highly correlated to the signal to noise ratio (SNR) of the CCD. The main contributor for the SNR is the temperature of the CCD. When the temperature goes up, the ability to extract mineral information goes down. This research cannot give a final conclusion as to the optimal temperature for the CCD as basic physics suggests that the lower the temperature the better the SNR. Clearly power usage of the cooling Peltier and the thermal environment of the RLS instrument within the instrument package will be a major issue in the overall design to the ExoMars Rover.

2.7 References

- Balkanski, M., R. F. Wallis, E. Haro, (1983), Anharmonic effects in light scattering due to optical phonons in silicon, *Phys. Rev. B* 28, p. 1928–1934.
- Bazalgette Courrèges-Lacoste, G., B. Ahlers, F. R. Pérez, (2007), Combined Raman spectrometer/laser-induced breakdown spectrometer for the next ESA mission to Mars, *Spectrochimica Acta Part A* 68, p. 1023–1028.
- Colin A. et al., (2012), Exploring the feasibility of determining soil water contents on the Moon with a combined Raman/LIBS instrument, *GeoRaman Xth Meeting, Nancy (France) – poster*.
- Denson, S. C., C. J. S. Pommier and M. B. Denton, (2007), The impact of array detectors on Raman spectroscopy. *Journal of chemical education*, Vol. 84, p. 67-74.
- Escudero-Sanz, I., B. Ahlers, G. B. Courrèges-Lacoste, (2008), Optical design of a combined Raman–laser-induced-breakdown-spectroscopy instrument for the European Space Agency ExoMars Mission, *Optical Engineering* 47(3), 033001-1, 033001-11.
- G. G. Harrigan, R. Goodacre, (2003), *Metabolic Profiling: Its Role in Biomarker Discovery and Gene Function Analysis*, Kluwer Academic Publisher, pp 337.
- Gillet P. et al., (2000), A thermodynamic model for MgSiO_3 perovskite derived from pressure, temperature and volume dependence of the Raman mode frequencies, *Physics of the Earth and Planetary Interiors*, Vol. 117, Issue 1-4, p. 361-384.
- Gillet, P. et al., (1993c), Phase changes and thermodynamic properties of CaTiO_3 . Spectroscopic data, vibrational modelling and some insights on the properties of MgSiO_3 perovskite. *Physics and Chemistry of Minerals*, Vol. 20, p. 159-170.
- Gillet, P., A. Lecleach and M. Madon, (1990), High-temperature Raman spectroscopy of the SiO_3 and GeO_2 polymorphs: anharmonicity and thermodynamic properties at high-temperature. *Journal of Geophysical Research- Solid Earth and Planets*, Vol. 95, p. 21635-21655.
- Gillet, P., C. Biellmann, B. Reynard and P. McMillan, (1993a), Raman spectroscopic studies of carbonates. Part I: High-pressure and high-temperature behaviour of calcite, magnesite, dolomite, aragonite. *Physics and Chemistry of Minerals*, Vol. 20, p. 1-18.
- Gillet, P., F. Guyot and J.M. Malezieux, (1989), High-pressure and high-temperature Raman spectroscopy of Ca_2GeO_4 : some insights on anharmonicity. *Physics of the Earth and Planetary Interiors*, Vol. 58, p. 141-154.
- Gillet, P., F. Guyot and Y. B. Wang, (1996a), Microscopic anharmonicity and equation of state of MgSiO perovskite. *Geophysical Research Letters*, Vol. 23, p. 3043-3046.

- Gillet, P., I. Daniel and F. Guyot, (1997), Anharmonic properties of Mg₂SiO₄-forsterite measured from the volume dependence of the Raman spectrum. *European Journal of Mineralogy*, Vol. 9, p. 255-262.
- Harris, R. D., D. A. Cremers, C. Khoo, K. Benelli, (2005), LIBS-based detection of geological samples at low pressures (<0.0001 Torr) for Moon and asteroid exploration. *LPS XXXVI*, 1796.
- Herzberg, G. (1945), *Molecular spectra and molecular structure: Infrared and Raman spectra of polyatomic Molecules*, Van Nostrand Reinhold Company, pp. 650.
- Knight, A. K., N. L. Scherbarth, D. A. Cremers, M. J. Ferris, (2000), Characterization of laser-induced breakdown spectroscopy (LIBS) for applications to space exploration. *Applied Spectroscopy*, Vol. 54, p. 331–340.
- Lasue, J. et al., (2012), Remote laser induced breakdown spectroscopy (LIBS) for lunar exploration. *Journal of Geophysical Research*, Vol. 117, Issue E1, CiteID E01002.
- Lazic, V. et al., (2007), Laser induced breakdown spectroscopy of soils, rocks and ice at sub-zero temperatures in simulated Martian conditions. *Spectrochimica Acta B*, Vol. 62, p. 1546-1556.
- Lenain, B. et al., (2007), Raman Spectroscopy for Process Control in Chemical and Pharmaceutical Manufacturing, *STP Pharma Techniques Pratiques Reglementations* Vol. 17, p. 171-174.
- Lewis, I. R. and H. Edwards, (2001), *Handbook of Raman Spectroscopy: from the research Laboratory to the process Line*. Practical Spectroscopy Series, Vol. 28, CRC Press.
- Lucazeau, G. (2003), Effect of pressure and temperature on Raman spectra of solids: anharmonicity. *Journal of Raman Spectrosc*, Vol. 34, p. 478–496.
- Mammone, J. F. and S. K. Sharma, (1979), Pressure and temperature dependence of the Raman spectra of rutile structure oxides. *Carnegie institution yearbook*, Vol. 78, p. 369-373.
- McCreery, R. L. (2000), Raman spectroscopy for Chemical Analysis. In: *A series of Monographs on Analytical Chemistry and its Applications* (J.D. Winefordner, editor), 157. Wiley-Interscience, John Wiley & Sons. Inc.
- Nakamoto, K. (1986), *Infrared and Raman spectra of inorganic and coordination compounds*.
- Pavlov, S.G., et al., (2011), Miniaturized laser induced plasma spectrometry for planetary in-situ analysis-the case for Jupiter's moon Europa. *Advances in Space Research* Vol. 48, p. 764-778.
- Raman, C.V. and K.S. Krishnan, (1928), A new type of secondary radiation. *Nature*, Vol. 121, p. 501-502.

- Rauschenbach, I., E. K. Jessberger, S. G. Pavlov, H. W. Hubers, (2010), Miniaturized LIBS for the in-situ analysis of the Martian surface: calibration and quantification. *Spectrochimica Acta B* 65, p. 758–768.
- Rayleigh, L. (1899), On the transmission of Light through an atmosphere containing small particles in susoension and on the origin of blue sky. *Philosophical Magazine Series 5*, Vol. 47, p. 375-384.
- Reynard. B, G. Montagnac and H. Cardone, (2012), Raman spectroscopy at high pressure and temperature for the study of the Earth's mantle and planetary minerals, *EMU Notes in Mineralogy*, Vol. 12, chapter 10, p. 367-390.
- Rull, F. (2012), The Raman effect and the vibrational dynamics of molecules and solids. In: application of Raman Spectroscopy to Earth Sciences and Cultural Heritage (J. Dubessy, M.-C. Caumon & F. Rull, editors). *EMU Notes in Mineralogy*, 12, European Mineralogical Union and the Mineralogical Society of Great Britain & Ireland, p. 1-60.
- Sallé, B. et al., (2004), Laser-Induced Breakdown Spectroscopy for Mars surface analysis: capabilities at stand-off distances and detection of chlorine and sulphur elements, *Spectrochimica Acta Part B: Atomic Spectroscopy* 59(9), p. 1413-1422.
- Sergey B. M. et al., (1999), A novel laser breakdown spectrometer for environmental monitoring, *Proc. SPIE* 3855, *Air Monitoring and Detection of Chemical and Biological Agents II*, 34, doi:10.1117/12.371277.
- Smekal, A. (1923), Zur Quantentheorie der Dispersion. *Naturwissenschaften*, 11, p. 873-875.
- Smith, E. and G. Dent, (2005), *Modern Raman spectroscopy, a practical approach*, John Wiley & Sons Inc, pp 224.
- Sobron, P., A. Wang, (2012), A planetary environment and analysis chamber (PEACH) for coordinated Raman–LIBS–IR measurements under planetary surface environmental conditions, *Vol. 43, Issue 2*, p. 212–227.
- Sutherland, G. B. B. M. (1933), Experiments on the Raman Effect at Very Low Temperatures, *Proceedings of the Royal Society of London. Series A, Containing Papers of a Mathematical and Physical Character*, Vol. 141, No. 845, p. 535-549.
- Thompson, J. R., et al., (2006), Remote Laser-Induced Breakdown Spectroscopy Analyses of Dar al Gani 476 and Zagami Martian Meteorites. *Journal of Geophysical Research*, v. 111, doi: 1029/2005JE002578.
- Wiens J. J., J. W. Fetzner, C. L. Parkinson, T. W. Reeder, (2005), Hylid frog phylogeny and sampling strategies for speciose clades. *Syst. Biol.* Vol. 54, p. 719–748.
- Willes, W. and R. Merlin, (editors) (2000), *Raman Scattering in Materials*. Springer Series in Materials Science, Vol. 42. Springer-Verlag.